Received November 15, 2017, accepted December 26, 2017, date of publication January 1, 2018,
date of current version February 28, 2018.

Digital Object Identifier 10.1109/ACCESS.2017.2788818

On Stability of Voltage Source Inverters in Weak Grids

ASWAD ADIB[1], (Student Member, IEEE), BEHROOZ MIRAFZAL[1], (Senior Member, IEEE), XIONGFEI WANG[2], (Senior Member, IEEE), AND FREDE BLAABJERG[2], (Fellow, IEEE)

[1]Department of Electrical and Computer Engineering, Kansas State University, Manhattan, KS 66506, USA
[2]Department of Energy Technology, Aalborg University, 9220 Aalborg, Denmark

Corresponding author: Behrooz Mirafzal (mirafzal@ksu.edu)

This work was supported by the U.S. National Science Foundation under Grant ECCS-1351665.

ABSTRACT As the number of inverters increases in the power grid, the stability of grid-tied inverters becomes an important concern for the power industry. In particular, a weak grid can lead to voltage fluctuations at the inverter terminals and consequently cause inverter instability. In this paper, impacts of circuit and control parameters on the stability of voltage source inverters are studied using a small-signal state-space model in the synchronously rotating *dq*-frame of reference. The full-order state-space model developed in this paper is directly extracted from the pulsewidth modulation switching pattern and enables the stability analysis of concurrent variations in the three-phase circuit and control parameters. This paper demonstrates that the full-order model of a grid-tied active (P) and reactive (Q) power (PQ)-controlled voltage source inverter (VSI) can be significantly reduced to a second-order model, preserving the overall system stability in the case of grid impedance variations. This paper also shows that a decrease in the grid inductance does not necessarily improve the stability of grid-tied VSIs. The system stability is a function of both the grid R/X ratio and grid inductance. Despite the grid-side inductor of the LCL filter is in series with the grid impedance, they have different impacts on the stability of a grid-tied PQ-controlled VSI, i.e., an increase in the filter inductance may improve the system stability in a weak grid. These findings are verified through simulated and experimentally obtained data.

INDEX TERMS Grid-tied voltage-source inverter, weak grids, microgrids, active (P) and reactive (Q) power (PQ)-controlled inverters, stability analysis, reduced-order model.

I. INTRODUCTION

The drive towards renewable resources is shifting energy production to distributed nodes, making the pulsewidth modulated (PWM) voltage source inverter (VSI) a widely used interface circuit between renewable sources and the grid [1], [2]. The widespread utilization of PWM inverters in the power grid makes the stability analysis of grid-tied VSIs a primary concern for power engineers. Several studies show that the stability of grid-tied VSIs is affected by the control and filter parameters [3]–[9]. Besides the filter and control parameters, a weak grid can adversely affect the stability of grid-tied VSIs [10]–[15]. A weak grid is commonly defined as a power grid with a low short-circuit ratio (SCR), i.e. high impedance, and a low inertia constant (H), which are typical features of microgrids. As a result, the voltage and frequency can be distorted in weak grids. Furthermore, the grid-tied VSI may become unstable if the voltage at the point of common coupling (PCC) has a harmonic component at the natural frequency of the LCL filter [10], [11]. The situation will be complicated even further if a voltage feedforward path is used to reduce the response time of the closed-loop system. Similarly, the coupling paths in the control scheme can drive the system towards instability in a grid with current harmonics [14], [15]. Hence, the stability analysis of inverters in weak grids is a complicated problem, requiring detailed dynamic models. The root-locus state-space and Nyquist impedance-based techniques have been reported for the stability analysis of grid-tied VSIs [9]–[19]. The impedance-based technique uses lumped equivalent circuits, and thus, the impact of individual circuit and control parameters on the system stability cannot be simply studied. In the dynamic analysis of grid-tied VSIs via state-space methods, a simplified model is typically considered either for the plant (circuit) or for the controller. This simplification makes the stability analysis of the overall system difficult if one needs to study the effect of concurrent variations in the circuit and control parameters.

In this paper, impacts of the grid, control scheme, and filter parameters on the stability of active (P) and reactive (Q) power (PQ)-controlled grid-tied VSIs are studied using a

twelfth-order state-space model. Also, a reduced-order model for grid-tied VSIs is developed using the balanced truncation technique. The reduced-order model will ease the computational complexity of microgrids with a large share of VSI-based generation units while preserving the stability feature of the full-order model [20]–[22]. The main findings of this paper are highlighted below:

- The full-order model of grid-tied closed-loop VSIs can be reduced to a second-order model, preserving the overall system stability.
- A decrease in the grid inductance does not necessarily improve the stability of grid-tied VSIs. The system stability is a function of both the grid R/X ratio and grid inductance.
- A decrease in the inductance of the grid-side LCL filter leads to instability even though the filter inductance is in series with the grid impedance, assuming that the current feedback sensor is located at the PCC.

The remainder of this paper is organized as follows. In Section II, the full-order closed-loop model of a PQ-controlled grid-tied VSI is derived, comprising the grid, filter, and control scheme dynamics. The root locus analysis is performed in Section III to investigate the effect of system parameters on system stability under weak grid conditions. Moreover, several scenarios discussed in Section III are experimentally verified in Section IV. In Section V, a reduced-order model of the grid-tied VSI is presented and also verified through time-domain simulation and eigenvalue analysis. Finally, a summary of findings is given in Section VI.

II. STATE-SPACE MODEL OF GRID-TIED VSI

In this section, the state-space model of the closed-loop grid-tied PQ-controlled VSI, which is shown in Fig. 1 is derived. While several state-space models for open-loop grid-tied VSIs can be found in literature, for the purpose of continuity and reproducibility of the work presented in this section, the open-loop model in [23] is concisely reconstructed and verified in Appendix A. Notice that the open-loop model for grid-tied VSIs is derived from the PWM switching pattern. The small-signal open-loop model is

$$\frac{d}{dt}\begin{bmatrix}\tilde{i}_{inv}\\ \tilde{v}_c\\ \tilde{i}_g\end{bmatrix}=\begin{bmatrix}A_{11} & A_{12} & A_{13}\\ A_{21} & A_{22} & A_{23}\\ A_{31} & A_{32} & A_{33}\end{bmatrix}\begin{bmatrix}\tilde{i}_{inv}\\ \tilde{v}_c\\ \tilde{i}_g\end{bmatrix}+\begin{bmatrix}0 & B_{12} & b_1\\ 0 & 0 & b_2\\ B_{31} & 0 & b_3\end{bmatrix}\begin{bmatrix}\tilde{v}_{pcc}\\ \tilde{u}\\ \tilde{\omega}\end{bmatrix} \quad (1)$$

where, $\tilde{i}_{inv}=\begin{bmatrix}\tilde{i}_q & \tilde{i}_d\end{bmatrix}^T$ is the inverter output current perturbation, $\tilde{v}_c=\begin{bmatrix}\tilde{v}_q & \tilde{v}_d\end{bmatrix}^T$ is the filter capacitor voltage, $\tilde{i}_g=\begin{bmatrix}\tilde{i}_q^g & \tilde{i}_d^g\end{bmatrix}^T$ is the grid current, and $\tilde{v}_{pcc}=\begin{bmatrix}\tilde{v}_q^{pcc} & \tilde{v}_d^{pcc}\end{bmatrix}^T$ is the voltage at the PCC. Furthermore, $\tilde{u}=\begin{bmatrix}\tilde{m} & \tilde{\psi}\end{bmatrix}^T$, where $\tilde{m}$ is the modulaion index and $\tilde{\psi}$ is the angle between Phase-A of the inverter's output voltage and the q-axis, see Fig. 2. Also, $\tilde{\omega}$ represents the grid's frequency variation. Again, further

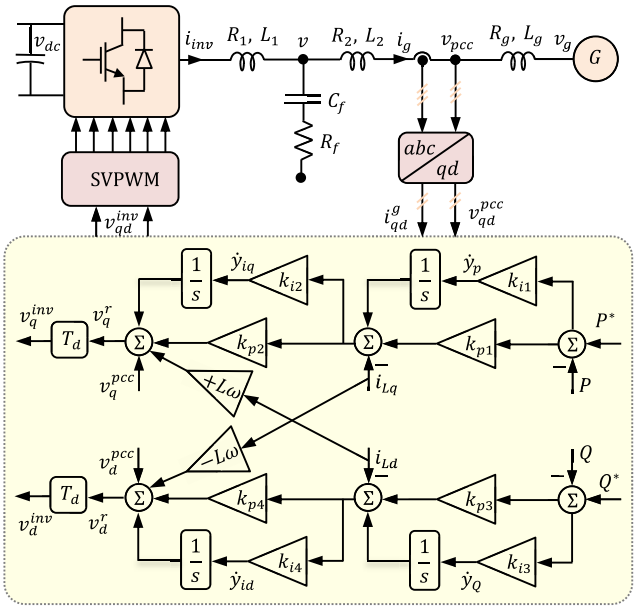

FIGURE 1. Control block diagram of a PQ-controlled grid-tied VSI.

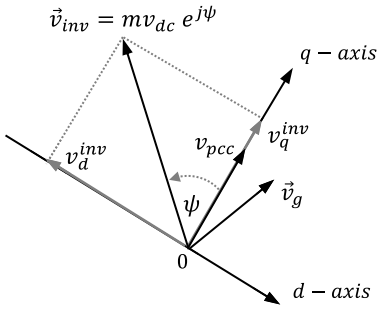

FIGURE 2. The inverter voltage plotted at *dq* axis.

details on the open-loop model are provided in Appendix A, and the block matrices introduced in (1) are all given in Appendix B.

For grid-tied VSIs, the PQ-control scheme is the most commonly implemented control strategy and hereby employed in this paper, whereas other control schemes might be required in an islanded mode to directly regulate the voltage at the PCC [24]–[26]. As illustrated in Fig. 1, the grid-side line-to-line voltages and line currents are sensed at the PCC and transformed to the dq-frame that are then used as inputs to the PQ-control schemes. The P and Q control loops are cascaded with q- and d- current control loops to independently control the active and reactive power, see Fig. 1. Accordingly, four new state variables, y_P, y_{iq}, y_Q, and y_{id}, must be added to the open-loop model in (1) with respect to the integrator blocks in the four PI controllers shown in Fig. 1. The state variables are then described by

$$\dot{y}_P = K_{I1}\left(P^* - P\right), \quad (2)$$
$$\dot{y}_{iq} = K_{I2}\left(y_P + K_{P1}\left(P^* - P\right) - i_{qL}\right), \quad (3)$$
$$\dot{y}_Q = K_{I3}\left(Q^* - Q\right), \quad (4)$$
$$\dot{y}_{id} = K_{I4}\left(y_Q + K_{P3}\left(Q^* - Q\right) - i_{dL}\right). \quad (5)$$

Here, P^* and Q^* are the desired values of the active and reactive power supplied to the grid, respectively. Also, at the PCC, the active and reactive power can be expressed in terms of the measured quantities as

$$P = \frac{1}{2}v_q^{pcc}i_{qL} + \frac{1}{2}v_d^{pcc}i_{dL}, \tag{6}$$

$$Q = \frac{1}{2}v_q^{pcc}i_{dL} - \frac{1}{2}v_d^{pcc}i_{qL}. \tag{7}$$

Using (2) through (7) and linearizing them around an operating point, the new state variables can be expressed in a matrix form as

$$\frac{d}{dt}\begin{bmatrix}\tilde{y}_1\\ \tilde{y}_2\end{bmatrix} = \begin{bmatrix}A_{43} & 0 & 0\\ A_{53} & A_{54} & 0\end{bmatrix}\begin{bmatrix}\tilde{i}_{gL}\\ \tilde{y}_1\\ \tilde{y}_2\end{bmatrix} + \begin{bmatrix}B_{41} & B_{43}\\ B_{51} & B_{53}\end{bmatrix}\begin{bmatrix}\tilde{v}_{pcc}\\ \tilde{R}^*\end{bmatrix}, \tag{8}$$

where, $\tilde{y}_1 = \begin{bmatrix}\tilde{y}_P & \tilde{y}_Q\end{bmatrix}^T$, $\tilde{y}_2 = \begin{bmatrix}\tilde{y}_{iq} & \tilde{y}_{id}\end{bmatrix}^T$ and $\tilde{R}^* = \begin{bmatrix}\tilde{P}^* & \tilde{Q}^*\end{bmatrix}^T$. The two new input variables are the desired active and reactive power of the system. The block matrices introduced in (8) are included in Appendix B. Also, using Fig. 1, the controller output equations are written as

$$v_q^r = v_q^{pcc} + K_{P2}\left(y_P + K_{P1}\left(P^* - P\right) - i_{qL}\right) + \omega L i_{dL} + y_{iq}, \tag{9}$$

$$v_d^r = v_d^{pcc} + K_{P4}\left(y_Q + K_{P3}\left(Q^* - Q\right) - i_{dL}\right) - \omega L i_{qL} + y_{id}. \tag{10}$$

Notice that the controller has been expressed in terms of line-to-line voltages and i_{qL} and i_{dL}, which are the dq-frame of reference counterparts of the *virtual* line-to-line currents, defining as $i_{ab} = i_a - i_b$, $i_{bc} = i_b - i_c$ and $i_{ca} = i_c - i_a$. The line currents can be expressed with respect to the virtual line-to-line currents in the dq-frame as

$$\begin{bmatrix}i_q^g\\ i_d^g\end{bmatrix} = \begin{bmatrix}\frac{1}{2} & \frac{-1}{2\sqrt{3}}\\ \frac{1}{2\sqrt{3}} & \frac{1}{2}\end{bmatrix}\begin{bmatrix}i_{qL}\\ i_{dL}\end{bmatrix} \tag{11}$$

It should be emphasized that the controller equations will remain unchanged if one chooses to use phase voltages and line currents instead of line-to-line voltages and virtual line-to-line currents. Therefore, the model derived in this section will be directly applicable for grid-tied VSIs with controllers using phase voltage and line current variables.

In the open-loop model, the voltage at the PCC was assumed as the input. To study the effect of the weak grid on the system stability, the grid circuit has to be included in the state-space model. To that end, the voltage at the PCC is expressed in terms of grid voltages as

$$v_q^{pcc} = R_g i_{qL} + L_g\frac{di_{qL}}{dt} + \omega L_g i_{dL} + v_q^g, \tag{12}$$

$$v_d^{pcc} = R_g i_{dL} + L_g\frac{di_{dL}}{dt} - \omega L_g i_{qL} + v_d^g. \tag{13}$$

Here, L_g and R_g are the grid inductance and resistance, respectively. The grid voltages can also be written in block matrix form as

$$v_{pcc} = G_1 i_{gL} + G_2\frac{di_{gL}}{dt} + v_g. \tag{14}$$

where G_1 and G_2 are defined in Appendix B. To insert the grid impedance into the system, the di_{gL}/dt term must be written in terms of state variables using (1) and (11), which yields

$$v_{pcc} = \left(I - G_2 B_{31}^L\right)^{-1}\left(G_2 A_{31}^L i_{inv} + G_2 A_{32}^L v_c + \left(G_1 + G_2 A_{33}^L\right) i_{gL} + G_2 b_3^L \omega + v_g\right) \tag{15}$$

The modified block matrices are presented in Appendix B.

A time delay in the controller can affect the stability of grid-tied inverters [27], [28], thus, the delay should be added to the state-space model. A simple way to implement the delay is through the following differential equations.

$$\dot{v}_q^{inv} = \frac{1}{T_d}\left(v_q^r - v_q^{inv}\right) \tag{16}$$

$$\dot{v}_d^{inv} = \frac{1}{T_d}\left(v_d^r - v_d^{inv}\right) \tag{17}$$

where, T_d is the control delay [27], [28], see Fig. 1. Substituting and linearizing v_q^r and v_d^r from (9) and (10) into (16) and (17) yields:

$$\frac{d}{dt}\tilde{v}_{inv} = A_{63}\tilde{i}_{gL} + A_{64}\tilde{y}_1 + A_{65}\tilde{y}_2 + A_{66}\tilde{v}_{inv} + B_{61}\tilde{v}_{pcc} + B_{63}\tilde{R}^* \tag{18}$$

where, $\tilde{v}_{inv} = \begin{bmatrix}\tilde{v}_q^{inv} & \tilde{v}_d^{inv}\end{bmatrix}^T$. The block matrices introduced can be found in Appendix B. On the other hand, from Fig. 2, v_q^{inv} and v_d^{inv} can be written in terms of m and ψ as

$$v_q^{inv} = m v_{dc}\cos(\psi), \tag{19}$$

$$v_d^{inv} = -m v_{dc}\sin(\psi). \tag{20}$$

After linearizing (19) and (20), $\tilde{u} = \begin{bmatrix}\tilde{m} & \tilde{\psi}\end{bmatrix}^T$ can be expressed as $\tilde{u} = M^{-1}\tilde{v}_{inv}$. Merging (1), (8) and (18), and substituting $\tilde{v}_{pcc}$ from (15) and $\tilde{u} = M^{-1}\tilde{v}_{inv}$, equation (21), as shown at the bottom of the next page, provides the closed-loop model of the grid-tied VSI system, where the associated block matrices are given in Appendix B. The model output equation is derived using (6), (7) and (15) and is also included in Appendix B. The eigenvalue analysis is performed in the next section based on the matrix given in (21) for the closed-loop VSI. Moreover, a phase detector (the so-called instantaneous PLL) can be used to obtain the reference angle at the PCC as defined below [24], [25]:

$$\theta = \tan^{-1}\left(\frac{v_{ab} + 2v_{bc}}{\sqrt{3}v_{ab}}\right) \tag{22}$$

where $d\theta/dt = \omega$ is the angular frequency of the grid. If a conventional PLL is used, PLL dynamics must be inserted into the model, where θ and ω become the new state variables [11]–[13].

TABLE 1. Simulation and experimental parameters.

Parameter	Value	Parameter	Value
v_{dc}	380 V	L_1	1 mH
v_{grid}	208 rms	R_1	0.15 Ω
C	1800 μF	L_2	0.5 mH
f_{pwm}	5 kHz	R_2	0.1 Ω
f	60 Hz	C_f	30 μF (Δ)

III. ROOT LOCUS ANALYSIS OF GRID-TIED CLOSED-LOOP VOLTAGE-SOURCE INVERTERS (VSIs)

In this section, the stability of the closed-loop grid-tied VSI is analyzed using the model developed in the previous section. In particular, impacts of a weak grid on the VSI stability are examined using eigenvalue analysis, when variations of the control time delay, T_d, passive damping, R_f, LCL filer and PQ-control parameters are taken into account. For the results presented in this section, the initial values of the hardware parameters are given in Table 1. Also, the control time delay is set to 0.3 ms and the coupling path gain is kept constant, $\omega L = 0.565\ \Omega$, see Fig. 1. Also, the PI controller gains in Fig. 4 are primarily set to $K_{p1} = K_{p3} = 0.01$, $K_{p2} = K_{p4} = 0.5$, $K_{i1} = K_{i3} = 2 - 10$, and $K_{i2} = K_{i4} = 5 - 10$. Herein, K_p values are chosen based on the initial system parameters, deliberately with a slight margin from unstable region for the root locus study. The LCL passive damping is initially assumed to be zero but the equivalent series resistance (ESR) of the 30 μF film capacitor is modeled by setting $R_f = 0.008\ \Omega$ for the frequency range of the case study.

In low-voltage distribution systems, the X_g/R_g ratio is around one. In Fig. 3, the root locus of the system's poles (eigenvalues) is shown as X_g/R_g ratio is gradually increased from 0.5 to 5 by increasing L_g from 0.16 mH to 1.6 mH, when $R_g = 0.12\ \Omega$. As shown in Fig. 3, increasing L_g drives a pair of poles, (λ_3, λ_4), toward unstable region, while the other poles stay stable. The system becomes unstable for $L_g > 1.12\ mH$, i.e. $X_g/R_g > 3.5$, and $SCR < 40$. If the X_g/R_g ratio is gradually increased from 0.5 to 5 by decreasing R_g from 0.12Ω to 0.012 Ω, where $L_g = 0.16\ mH$, the system becomes stable for $R_g > 0.064\ \Omega$, as shown in Fig. 4. Therefore, both L_g and R_g determine the weakness of a low-voltage grid.

For the control scheme shown in Fig. 1, increasing the time delay of feedback control paths or adding a series resistor

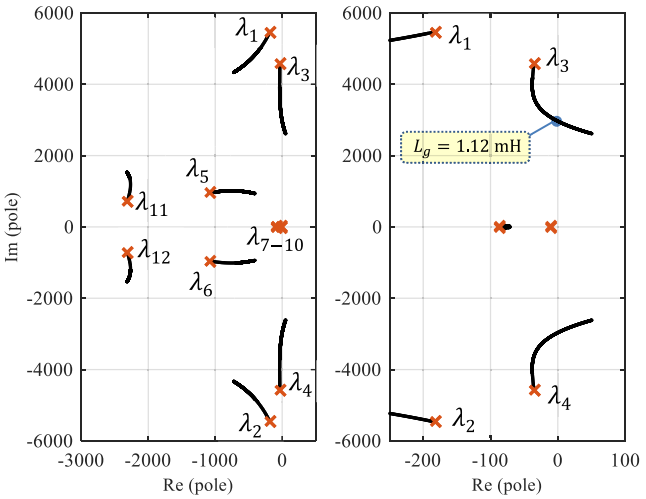

FIGURE 3. The root locus of the grid-tied closed-loop VSI system when L_g varies from 0.16 to 1.6 mH and $R_g = 0.12\Omega$ is kept constant (left), with a zoomed-in plot of the dominant poles (right).

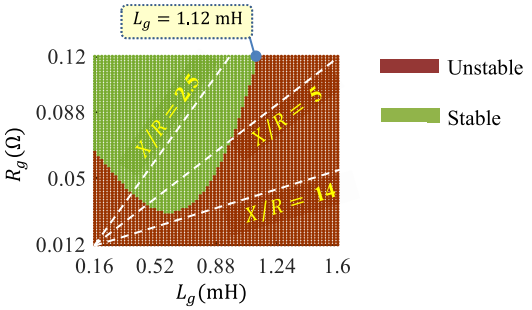

FIGURE 4. The stable and unstable regions with respect to the grid resistance and inductance values for the given system parameters.

to each capacitor in the LCL filter have similar effects on the stability of grid-tied VSIs. To demonstrate their impacts, the root loci of a dominant pole, λ_3, are plotted in Fig. 5 for two different scenarios; initially the grid inductance increases from 0.16 to 1.6 mH, as shown also in Fig. 3, followed by an increase in T_d or R_f. In the left side of Fig. 5, a time delay is added, where the system becomes stable for $T_d > 0.33\ ms$, while in the right side, a passive damping is added to the LCL filter to make the system stable for $R_f > 0.36\ \Omega$. However, adding a resistive element adversely affects the performance of the LCL filter, so it cannot be increased without a restraint. Therefore, the control and hardware designs should concurrently be done to achieve an efficient and robust system.

$$\frac{d}{dt}\begin{bmatrix} i_{inv} \\ v_c \\ i_{gL} \\ y_1 \\ y_2 \\ v_{inv} \end{bmatrix} = \begin{bmatrix} A_{11} & A_{12} & A^L_{13} & 0 & 0 & A^C_{16} \\ A_{21} & A_{22} & A^L_{23} & 0 & 0 & 0 \\ A^C_{31} & A^C_{32} & A^C_{33} & 0 & 0 & 0 \\ A^C_{41} & A^C_{42} & A^C_{43} & 0 & 0 & 0 \\ A^C_{51} & A^C_{52} & A^C_{53} & A_{54} & 0 & 0 \\ A^C_{61} & A^C_{62} & A^C_{63} & A_{64} & A_{65} & A_{66} \end{bmatrix} \begin{bmatrix} i_{inv} \\ v_c \\ i_{gL} \\ y_1 \\ y_2 \\ v_{inv} \end{bmatrix} + \begin{bmatrix} 0 & b_1 & 0 \\ 0 & b_2 & 0 \\ B^C_{31} & b^C_3 & 0 \\ B^C_{41} & b^C_4 & B_{43} \\ B^C_{51} & b^C_5 & B_{53} \\ B^C_{61} & b^C_6 & B_{63} \end{bmatrix} \begin{bmatrix} v_g \\ \omega \\ R^* \end{bmatrix} \tag{21}$$

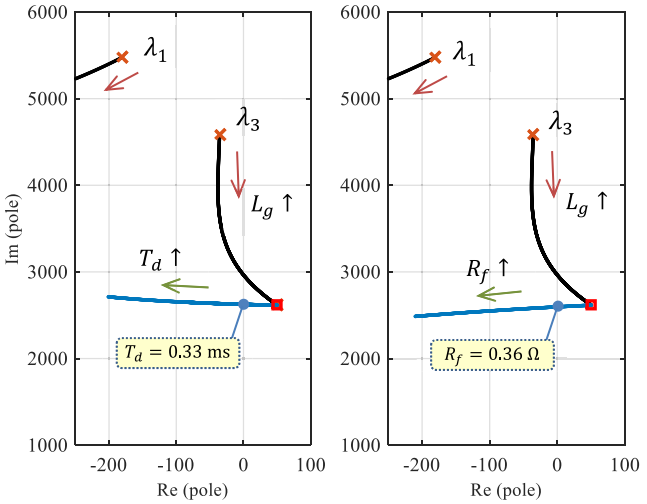

FIGURE 5. The root loci of λ_3 of the grid-tied closed-loop VSI system when initially L_g increases from 0.16 to 1.6 *mH*, followed by an increase in T_d from 0.3 to 0.4 *ms* (left), an increase in R_f from 0.008 to 2Ω (right).

It should be noted that if the L_1 current or inverter side current instead of the grid current was employed in the PQ control block diagram in Fig. 1, an increase in T_d would make the system unstable [28].

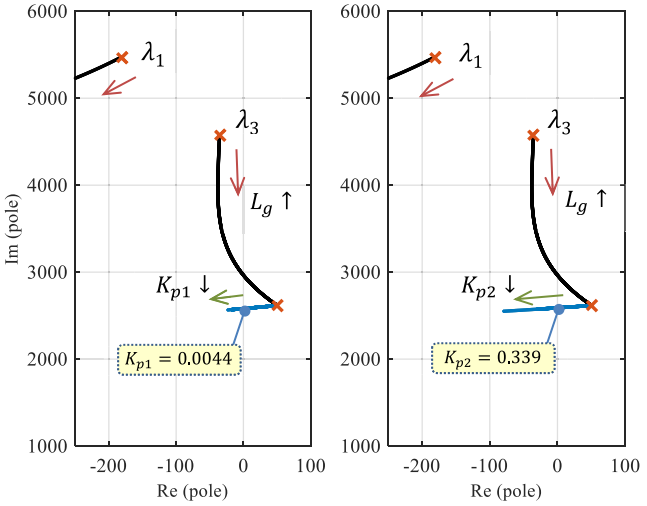

FIGURE 6. The root loci of λ_3 of the grid-tied closed-loop VSI system when initially L_g increases from 0.16 to 1.6 *mH*, followed by a decrease in K_{p1} from 0.01 to 0.001 (left), a decrease in K_{p2} from 0.5 to 0.05 (right).

The system stability is normally tuned by the control gains. As shown in the control schemes in Fig. 1, four K_ps and four K_is are implemented in the control block diagram. However, for a relatively wide range of variations in each K_i, all poles stay stable where indeed the dynamics performance, e.g. settling-time and steady-state error, is affected by K_i values. Moreover, the root loci of the system obtained from variations of the proportional coefficients, K_ps, show similar behaviors. With these remarks in mind, Fig. 6 demonstrates the system root loci for a decrease in K_{p1} from 0.01 to 0.001 (in left), and similarly a decrease in K_{p2} from 0.5 to 0.05. As can be seen, for $K_{p1} < 0.0044$ or $K_{p2} < 0.339$, the dominant pole, λ_3, moves back to stable region. This means that the system can be kept stable in a weak grid by decreasing the K_p gains. However, if the grid inductance becomes significantly large, adjusting the control parameters may not effectively prevent instability in the system. Furthermore, low K_p values can adversely affect the performance of the controller.

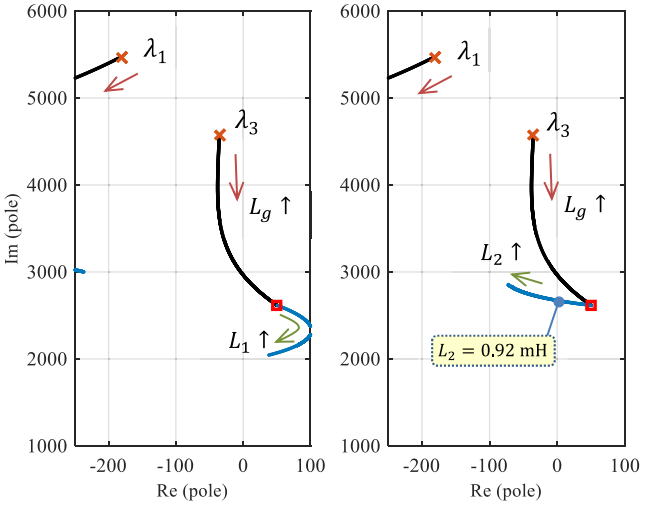

FIGURE 7. The root loci of λ_3 of the grid-tied closed-loop VSI system when initially L_g increases from 0.16 to 1.6 *mH*, followed by an increase in L_1 from 1 to 5 *mH* (left), an increase in L_2 from 0.5 to 5 *mH* (right).

Under stiff grid conditions, the LCL filter might be designed regardless of the grid impedance, but the same cannot be done for VSIs connected to a weak grid. The impacts of LCL filter parameters on the system stability are demonstrated in Fig. 7. In this figure, the system root loci are shown for two scenarios, again after the grid inductance is elevated from 0.16 to 1.6 mH. In the first scenario shown in Fig. 7 (left), L_1 increases from its initial value of 1 to 5 mH. In the second scenario shown in Fig. 7 (right), L_2 increases from its initial value of 0.5 to 5 mH. Notice, increasing $L_2(> 0.92\ mH)$ moves the system poles back to the left-side (stable) plane. Although L_2 is in series with L_g, remarkably an increase in L_2 benefits for the system stability. This is true only for grid-tied VSIs in which the voltage at the PCC is fed back to the controller either indirectly through the calculated active power and/or directly via the feedforward path shown in Fig. 1.

It can be observed from the eigenvalue analysis that one pair of poles, i.e. λ_3 and by association its complex conjugate pair λ_4, dominates the stability of a grid-tied inverter, thus based on the developed model, a second-order model is presented in a later section to make the stability analysis of microgrids less complicated.

IV. EXPERIMENTAL VERIFICATIONS

In this section, some of the findings discussed in the previous section are verified through laboratory experiments.

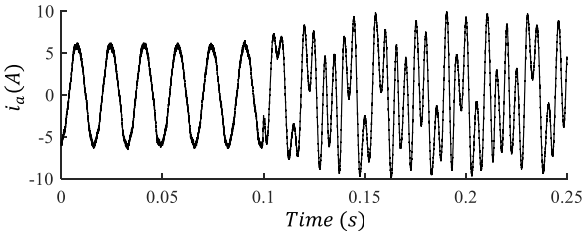

FIGURE 8. Line current injected to the grid while a 5*mH* inductor is added per phase to the grid impedance at 0.1 second.

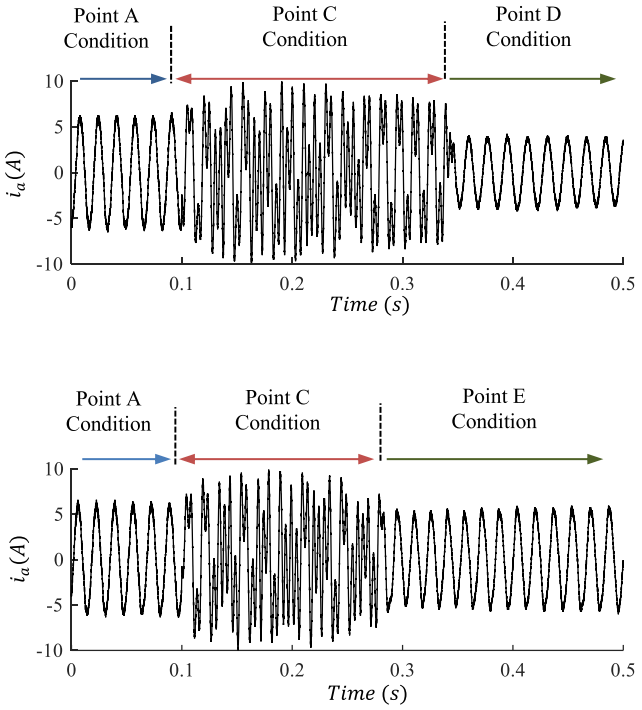

FIGURE 9. Line current flowing from the VSI to the grid with a grid impedance of 5*mH* added at 0.1*s* followed by inserting a 2.5*mH* inductor to L_2 at about 0.33 second (top), and inserting a $R_f = 10\Omega$ at about 0.29 second (bottom).

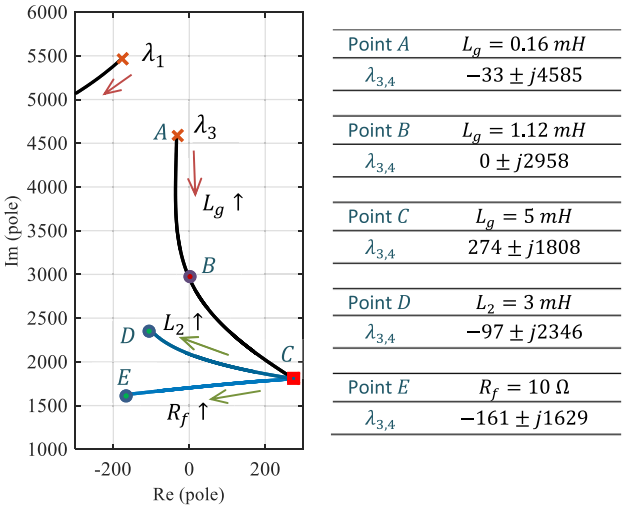

Point A	$L_g = 0.16\ mH$
$\lambda_{3,4}$	$-33 \pm j4585$
Point B	$L_g = 1.12\ mH$
$\lambda_{3,4}$	$0 \pm j2958$
Point C	$L_g = 5\ mH$
$\lambda_{3,4}$	$274 \pm j1808$
Point D	$L_2 = 3\ mH$
$\lambda_{3,4}$	$-97 \pm j2346$
Point E	$R_f = 10\ \Omega$
$\lambda_{3,4}$	$-161 \pm j1629$

FIGURE 10. System root locus of the dominant eigenvalue, λ_3, when the grid inductance increases to 5 *mH* at point C, followed by two different scenarios (*i*) an increase in L_2 up to 3 *mH* at point D, and (*ii*) an increase R_f up to 10Ω at point E.

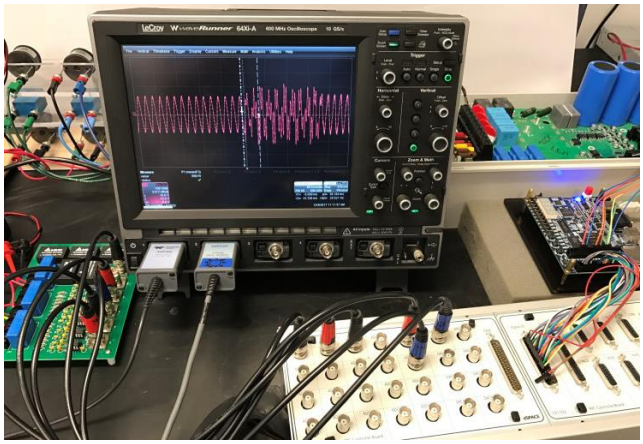

FIGURE 11. Experimental setup and scope display for the case study demonstrated in Fig. 9 (bottom).

The hardware and control schemes described in the previous sections were used for these experiments. The initial filter values chosen for the setup were $L_1 = 1\ mH$, $L_2 = 0.5\ mH$, $C_f = 30\ \mu F$, $R_f = 0\ \Omega$, when the closed-loop proportional gains were $K_{p1} = K_{p3} = 0.01$, and $K_{p2} = K_{p4} = 0.5$ for a stiff grid condition. However, the integral gains, K_is, were set to be small to prevent overshoots at the price of increasing the settling time. The first test scenario was designed to examine the impact of weak grid on the system stability. In this test, 5 *mH* inductors were inserted to the circuit right after the measurement points at the PCC, where they were intially bypassed through a three-phase switch. Fig. 8 shows the phase current injected to the grid when the system becomes unstable after adding the three line inductors. This experiment demonstrates how the VSI becomes unstable under a weak grid condition. Fig. 9 shows two different test scenarios when intially the system was stable (Point A in Fig. 10), then the line inductors were added to the grid impedance at $t = 0.1$s to make the system unstable (Point C in Fig. 10). In Fig. 9 (top), the system becomes stable at $t = 0.33\ s$ by inserting a 2.5 *mH* line inductor to the system that increases the value L_2 to 3 *mH* (representing Point D in Fig. 10). This is in agreement with the eigenvalue analysis discussed in the previous section as well as the model root locus of the dominant pole in Fig. 10. Notice that the magnitude of the current is initially smaller than its original value, after recovering at $t = 0.33$ s, while the controller is slowly restoring the current to its original value. In Fig. 9 (bottom), the system becomes stable at $t = 0.29$ s by inserting an R_f of 10 Ω, as also expected from the root locus plot at Point E in Fig. 10. In Fig. 11, the scope screen and the test setup for the second scenario is shown. These tests further confirm the practicality of employing the developed model in (21) for the design and dynamic behavior analysis of grid-tied VSIs.

V. REDUCED-ORDER MODEL

The twelfth-order model developed in (21) is suitable for the design and stability analysis of single grid-tied inverters as demonstrated and verified in the previous sections. However, the use of a comprehensive model might become cumbersome for microgrids with a large share of inverter-based distributed generation units. Hence, a lower-order model through model-order reduction techniques is necessary that preserves the stability of the system for concurrent variations in circuit and control parameters. Various techniques exist in literature to reduce the order of large dynamic systems. In power systems, the singular perturbation and Krylov subspace methods have been widely used [20], [21], [29]. In these two methods, a reduced-order model is derived to preserve the dynamic behavior of all slow poles, [20], [21], [29]. However, from the analysis presented in Section III, the dominant poles, i.e., λ_3 and λ_4, are only a subset of system's slow dynamics. Therefore, the aforementioned methods might not be the most suitable ones in obtaining a second-order model for the system presented in (21). A technique called *balanced truncation method* can identify the minimum state variables needed to preserve the dynamics behavior of the system regardless of their corresponding response time constants [30]. Notice that the balanced truncation method does not preserve the original state-space variables. In this section, the balanced truncation method is therefore applied to derive a second-order model for the grid-tied PQ-controlled VSIs, as shown in Fig. 1.

The first step in the balanced truncation technique is to transform the system to a so-called balanced form. This is achieved by applying a mathematical transformation, i.e., $\hat{x} = Tx$, where x and $\hat{x}$ are vectors of the original and new state variables, respectively, and T is the transformation matrix. The full-order state-space model in balanced form is then given by

$$\dot{\hat{x}} = TAT^{-1}\hat{x} + TBv \quad \text{and} \quad y = CT^{-1}\hat{x} + Dv \tag{23}$$

where, A, B, C and D are the corresponding state-space matrices of the full-order model. Also, v and y represent the input and output vectors of full-order model. The transformation matrix, T, must be selected such that the controllability and observability Gramians of (23) become equal and diagonal, i.e.,

$$\hat{\mathcal{P}} = T\mathcal{P}T' = \hat{\mathcal{Q}} = T'^{-1}\mathcal{Q}T^{-1} = \mathcal{H} \tag{24}$$

where $\mathcal{P}$ and $\hat{\mathcal{P}}$ are the controllability Gramians of the full-order model before and after the balancing transformation, respectively, and similarly, $\mathcal{Q}$ and $\hat{\mathcal{Q}}$ are defined as the observability Gramians. Herein, $\mathcal{H}$ is a diagonal matrix where the diagonal elements are the *Hankel singular values* [30]. By definition, a Hankel singular value indicates the contribution of each new state to the system input/output behavior. The states with the smaller Hankel singular values are the least controllable and observable, and therefore can be truncated without affecting system input/output response. The normalized Hankel singular values of the full-order model in (21) for the operating point specified in Section III are shown in Fig. 12. As one can see from Fig. 12, two of the states have significantly higher singular values and contain most of the system information compared to the rest of the states. This means a second-order model can represent the stability behavior of grid-tied VSIs that is also in agreement with the observations presented in Section III.

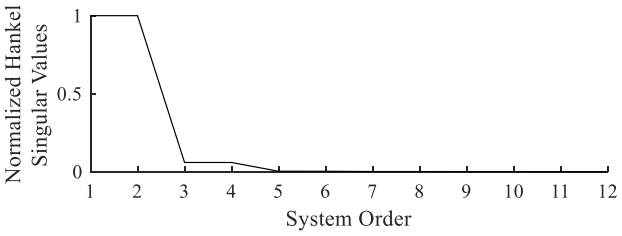

FIGURE 12. Normalized Hankel singular values versus the system order for a full-order grid-tied VSI.

By partitioning the system into two groups according to their Hankel singular values, the balanced state-space model in (23) can be expressed as

$$\begin{bmatrix} \dot{\hat{x}}_g \\ \dot{\hat{x}}_z \end{bmatrix} = \begin{bmatrix} \hat{A}_g & \hat{A}_{gz} \\ \hat{A}_{zg} & \hat{A}_z \end{bmatrix} \begin{bmatrix} \hat{x}_g \\ \hat{x}_z \end{bmatrix} + \begin{bmatrix} \hat{B}_g \\ \hat{B}_z \end{bmatrix} v$$
$$\text{and } y = \begin{bmatrix} \hat{C}_g & \hat{C}_z \end{bmatrix} \begin{bmatrix} \hat{x}_g \\ \hat{x}_z \end{bmatrix} + \hat{D}v \tag{25}$$

Now, trimming the states with smaller Hankel singular values [30], i.e. $\hat{x}_z$, the second-order model of the grid-tied PQ-controlled VSI can be reduced to

$$\dot{\hat{x}}_g = \hat{A}_g\hat{x}_g + \hat{B}_g v, \quad \text{and} \quad y = \hat{C}_g\hat{x}_g + \hat{D}v. \tag{26}$$

For example, the $\hat{A}_g$, $\hat{B}_g$, $\hat{C}_g$ and $\hat{D}$ matrices of the reduced-order model of the system specified in Section III can be obtained as

$$\hat{A}_g = \begin{bmatrix} -34.83 & 4429.11 \\ -4407.75 & -28.05 \end{bmatrix},$$
$$\hat{B}_g = \begin{bmatrix} -32.29 & 207.67 & -4.42 & 0.09 & 0.50 \\ -198.48 & -28.60 & -16.80 & -0.51 & 0.08 \end{bmatrix},$$
$$\hat{C}_g = \begin{bmatrix} 34.97 & 455.74 \\ -442.39 & 94.19 \end{bmatrix},$$
$$\hat{D} = \begin{bmatrix} -1.59 & 21.61 & -0.31 & 1.01 & 0.05 \\ -20.59 & 1.68 & -1.76 & -0.05 & 1.02 \end{bmatrix}.$$

This reduced-order model can be verified through time-domain circuit simulations in MATLAB/Simulink platform making use of the SimPowerSystems toolbox. To compare the dynamic behavior of the twelfth-order model with the second-order model, a step change on the desired active power is implemented followed by a step change in the desired reactive power, as shown in Fig. 13. It can be seen from Fig. 13 that the output of the reduced-order model is in good agreement with both the simulation values and the full-order model. Notice that only impacts of high-frequency modes, λ_3 and λ_4, are seen in this 2nd-order model. To prove

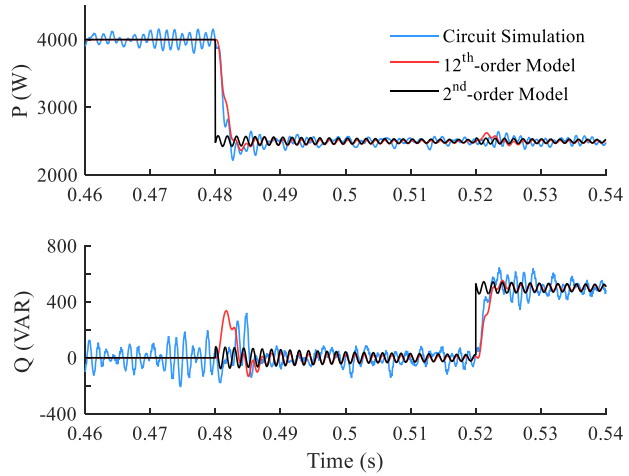

FIGURE 13. Time domain verification of the reduced-order model for a change in desired active power from 4 to 2.5 *kW* at $t = 0.48s$, followed by a change in desired reactive power from 0 to 500*VAR* at $t = 0.52s$.

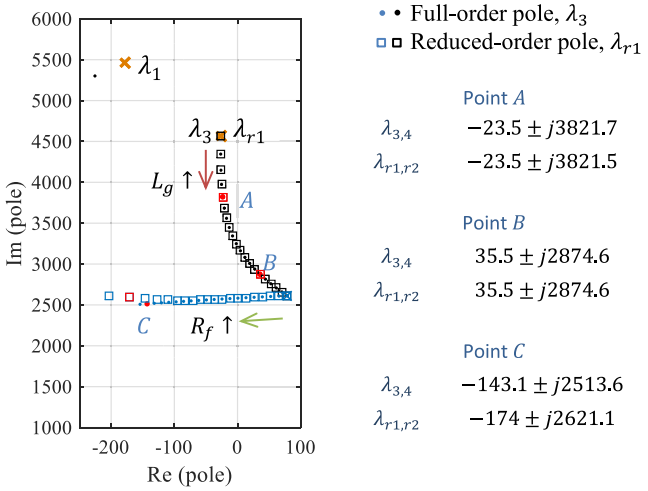

FIGURE 14. System root locus of the full-order dominant eigenvalue, λ_3 and reduced-order eigenvalue, λ_{r1}, when initially L_g increases from 0.16 *mH* to 1.6 *mH* followed by an increase in R_f from 0.008 Ω to 2 Ω.

the validity of the reduced-order approach for different operating points, the root locus of one of the dominant eigenvalues is compared against the root locus of the eigenvalue of the reduced-order model in Fig. 14 for the scenario shown in Fig. 5(right). It can be seen from Fig. 14 that eigenvalues of the full-order and reduced-order models completely overlap with each other in an unstable region and even in the stable region close to the imaginary axis. Two such points, point A and point B, are highlighted in Fig. 14 and it can be seen that the eigenvalues, λ_3 and λ_{r1}, of these models have the same trajectory due the circuit parameter changes. The eigenvalues of the two models are not exactly equal as the dominant eigenvalues move further into the stability region and in the neighborhood of other eigenvalues. However, the reduced-order model is able to predict the system stability with full accuracy, and therefore, provides a reliable indicator for the stability analysis of the grid-tied VSIs. Hence, the derived reduced-order model will be useful for the stability analysis of microgrids with a high share of inverter-based distributed generation units.

VI. CONCLUSION

In this paper, the stability of grid-tied PQ-controlled VSIs has been studied under weak grid conditions using a small-signal state-space model in the synchronously rotating *dq* reference frame. The model of the closed-loop system has been derived replacing the open-loop control inputs by the closed loop control inputs, which are the desired active and reactive power, and integrating state variables associated with the controller. The small-signal model has been used to analyze the system stability through eigenvalue trajectories. A number of scenarios have been investigated to understand impacts of circuit and control parameter variations on the grid-tied VSI stability. It has been demonstrated in this paper that how the inverter system moves to stable or unstable region as the grid impedance increases depending on the grid R/X ratio. It has been further demonstrated that an unstable grid-tied VSI under weak grid conditions can be made stable through an increase in grid-side LCL filter, controller time delay, passive damping resistance or a decrease in proportional controller parameters. In addition, the findings obtained from the developed model concerning the stability of grid-tied inverters in weak grids have been experimentally verified in this paper. Furthermore, it has been demonstrated that a pair of poles of the closed-loop system dominate the stability of the overall system. Following that analysis, a second-order model of the grid-tied VSI system has been derived using the balanced truncation method. The reduced-order model has been verified through simulation studies in the time domain. The developed second-order model will be useful for stability analysis of VSIs in weak grids. The technique presented in Section II and Appendix A, can be applied for any type of inverter and different control schemes, e.g., proportional resonant (PR) controllers, etc.

APPENDIX A

In this appendix, the state-space representation of an open-loop grid-tied VSI is derived. This is included only for the purpose of continuity and reproducibility of the work presented in this paper. The model is obtained in three steps. First, the state-space equations for the circuits corresponding to each switching state are derived. Notice while the space vector pulse width modulation (SVPWM) switching technique is used to derive the averaged state-space model, the resulting model is also valid for the sinusoidal plus third harmonic PWM (SPWM+3rdH) technique [31]. In the SVPWM technique, six sectors are defined containing six active {(100) , (110) , (010) , (011) , (001) , (101)} and two zero {(111) , (000)} switching states. Notice that the status of the top three switches is sufficient to show the switching state of a two-level inverter since at any instant only one switch from each leg is ON in order to prevent dc-bus short circuits. For example, the (100) switching state means the top switch connected to Phase-A and the bottom switches connected to Phase-B and -C are ON, while the other switches stay OFF.

TABLE 2. State-space model derivation steps for sector I of SVPWM in *abc* frame of reference.

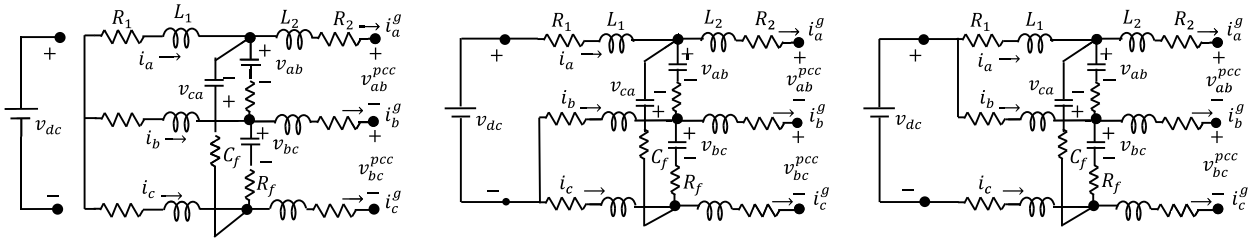

$\dot{x}_{abc} = A_0 x_{abc} + B u_{abc}$	$\dot{x}_{abc} = A_1 x_{abc} + B u_{abc}$	$\dot{x}_{abc} = A_2 x_{abc} + B u_{abc}$

$$\dot{x}_{abc} = \bar{A}_I + B u_{abc}\ , \qquad x_{abc} = \left[i_a \ \ i_b \ \ v_{ab} \ \ v_{bc} \ \ i_a^g \ \ i_b^g\right]^T , \qquad u_{abc} = \left[v_{dc} \ \ v_{ab}^{pcc} \ \ v_{bc}^{pcc}\right].$$

$$\bar{A}_I = \begin{bmatrix} \frac{-3R_1-R_f}{3L_1} & 0 & \frac{-2}{3L_1} & \frac{-1}{3L_1} & \frac{R_f}{3L_1} & 0 \\ 0 & \frac{-3R_1-R_f}{3L_1} & \frac{1}{3L_1} & \frac{-1}{3L_1} & 0 & \frac{R_f}{3L_1} \\ \frac{1}{3C_f} & \frac{-1}{3C_f} & 0 & 0 & \frac{-1}{3C_f} & \frac{1}{3C_f} \\ \frac{1}{3C_f} & \frac{2}{3C_f} & 0 & 0 & \frac{-1}{3C_f} & \frac{-2}{3C_f} \\ \frac{R_f}{3L_2} & 0 & \frac{2}{3L_2} & \frac{1}{3L_2} & \frac{-3R_2-R_f}{3L_2} & 0 \\ 0 & \frac{R_f}{3L_2} & \frac{-1}{3L_2} & \frac{1}{3L_2} & 0 & \frac{-3R_2-R_f}{3L_2} \end{bmatrix} \qquad B = \begin{bmatrix} \frac{2d_1+d_2}{3L_1} & 0 & 0 \\ \frac{-d_1+d_2}{3L_1} & 0 & 0 \\ 0 & 0 & 0 \\ 0 & 0 & 0 \\ 0 & \frac{-2}{3L_2} & \frac{-1}{3L_2} \\ 0 & \frac{1}{3L_2} & \frac{-1}{3L_2} \end{bmatrix}$$

In each sector, the inverter switching circuit alternates between a zero and two active switching states [31]. The three switching states of each sector result in three circuits, and thus, three distinct state-space equations. The circuit diagrams corresponding to the three switching states of Sector I, i.e. {(111) *or* (000)}, (100) and (110), are shown from left to right in Table 2. In the second step, these equations are averaged over the switching interval,

$$\frac{d}{dt}\begin{bmatrix} i_q \\ i_d \\ v_q \\ v_d \\ i_q^g \\ i_d^g \end{bmatrix} = \begin{bmatrix} \frac{-3R_1-R_f}{3L_1} & -\omega & \frac{-1}{2L_1} & \frac{\sqrt{3}}{6L_1} & \frac{R_f}{3L_1} & 0 \\ \omega & \frac{-3R_1-R_f}{3L_1} & \frac{-\sqrt{3}}{6L_1} & \frac{-1}{2L_1} & 0 & \frac{R_f}{3L_1} \\ \frac{1}{2C_f} & \frac{\sqrt{3}}{6C_f} & 0 & -\omega & \frac{-1}{2C_f} & \frac{-\sqrt{3}}{6C_f} \\ \frac{-\sqrt{3}}{6C_f} & \frac{1}{2C_f} & \omega & 0 & \frac{\sqrt{3}}{6C_f} & \frac{-1}{2C_f} \\ \frac{R_f}{3L_2} & 0 & \frac{1}{2L_2} & \frac{-\sqrt{3}}{6L_2} & \frac{-3R_2-R_f}{3L_2} & -\omega \\ 0 & \frac{R_f}{3L_2} & \frac{\sqrt{3}}{6L_2} & \frac{1}{2L_2} & \omega & \frac{-3R_2-R_f}{3L_2} \end{bmatrix} \begin{bmatrix} i_q \\ i_d \\ v_q \\ v_d \\ i_q^g \\ i_d^g \end{bmatrix} + \begin{bmatrix} \frac{\sqrt{3}mcos(\psi)}{3L_1} & 0 & 0 \\ \frac{-\sqrt{3}msin(\psi)}{3L_1} & 0 & 0 \\ 0 & 0 & 0 \\ 0 & 0 & 0 \\ 0 & \frac{-1}{2L_2} & \frac{\sqrt{3}}{6L_2} \\ 0 & \frac{-\sqrt{3}}{6L_2} & \frac{-1}{2L_2} \end{bmatrix} \begin{bmatrix} v_{dc} \\ v_q^{pcc} \\ v_d^{pcc} \end{bmatrix} \tag{A1}$$

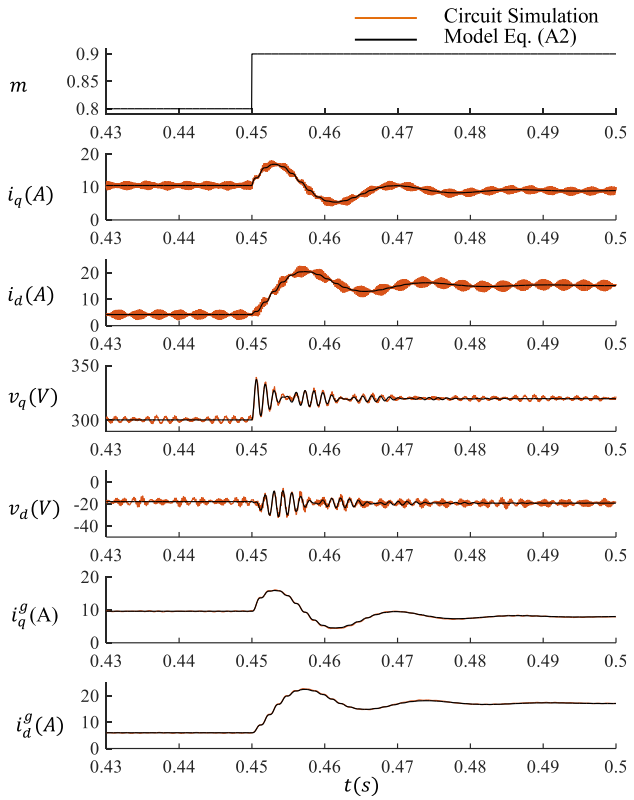

FIGURE 15. Three-phase two-level VSI model verification through simulation under a change in modulation index, *m*, from 0.8 to 0.9 at 0.45 second.

T_s to obtain a time-invariant state-space model [32], [33]. In these equations, $d_0(d_0 = t_0/T_s)$, $d_1(d_1 = t_1/T_s)$, and $d_2(d_2 = t_2/T_s)$ are the duty cycles for the zero switching state and the two active switching states, respectively, where $t_0 + t_1 + t_2 = T_s$. The derived state-space representation is only for Sector I. Following the same mathematical procedure, state-space representations of all six sectors are obtained. Finally, transferring all six state-space equations to the synchronously rotating reference frame, i.e. Park's transformation $x_{dq0} = Px_{abc}$ [34], [35], remarkably results in a single dynamic model for all six sectors that is given in (A1), as shown at the bottom of the previous page. As shown in (A1), the state-space matrix contains m and ψ as constant parameters which are control parameters (directly in the SPWM or indirectly in SVPWM technique), and therefore, vary by control signals of the system rather than being constant quantities, and thus, the time-invariant state-space model presented in (A1) actually describes a nonlinear system. Furthermore, it is expected that the fundamental frequency of the system is also an input rather than being a constant quantity. Thus, to obtain the small-signal model of the system, (A1) must be linearized around a steady-state operating point. The A matrix of the small-signal model is the same as that of the large-signal model. However, the B matrix in the small-signal model has three additional columns associated with the new inputs, $\tilde{m}$ and $\tilde{\psi}$, where $m = \tilde{m} + M$, $\psi = \tilde{\psi} + \Psi$ and $\omega = \tilde{\omega} + \Omega$. The steady-state values,

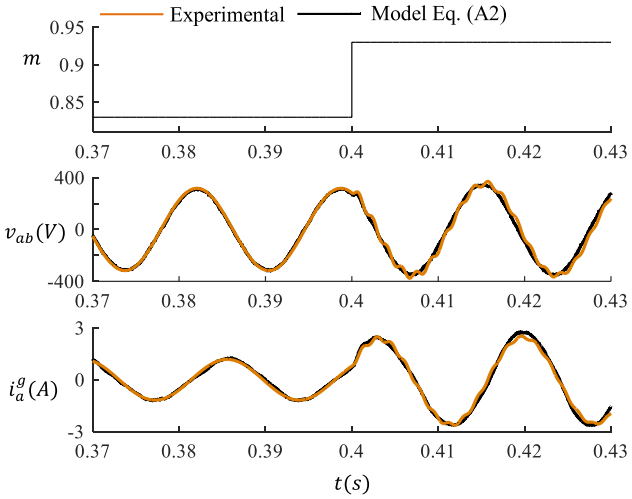

FIGURE 16. Three-phase two-level VSI model verification through experiment in the *abc* frame of reference.

M and Ψ, can be calculated for any given operating point using the active and reactive power generated by the inverter. Therefore, the new input vector is $\left[\tilde{v}_q^{pcc} \;\; \tilde{v}_d^{pcc} \;\; \tilde{m} \;\; \tilde{\psi} \; \tilde{\omega}\right]^T$ with the state variables replaced by their small-signal counterparts, e.g. $\tilde{x} = \left[\tilde{i}_q \;\; \tilde{i}_d \;\; \tilde{v}_q \;\; \tilde{v}_d \;\; \tilde{i}_q^g \;\; \tilde{i}_d^g\right]^T$. Notice that, v_{dc} has been considered as a constant voltage source, hence $\tilde{v}_{dc} = 0$. This constant dc voltage can be assumed when the inverter is in PQ-controlled mode, for example, in grid-tied battery energy storage systems. The resulting small-signal model can be expressed as

$$\frac{d}{dt}\begin{bmatrix}\tilde{i}_{inv}\\ \tilde{v}_c\\ \tilde{i}_g\end{bmatrix} = \begin{bmatrix}A_{11} & A_{12} & A_{13}\\ A_{21} & A_{22} & A_{23}\\ A_{31} & A_{32} & A_{33}\end{bmatrix}\begin{bmatrix}\tilde{i}_{inv}\\ \tilde{v}_c\\ \tilde{i}_g\end{bmatrix} + \begin{bmatrix}0 & B_{12} & b_1\\ 0 & 0 & b_2\\ B_{31} & 0 & b_3\end{bmatrix}\begin{bmatrix}\tilde{v}_{pcc}\\ \tilde{u}\\ \tilde{\omega}\end{bmatrix} \quad \text{(A2)}$$

where, $\tilde{i}_{inv} = \left[\tilde{i}_q \;\; \tilde{i}_d\right]^T$; $\tilde{v}_c = \left[\tilde{v}_q \; \text{`}\tilde{v}_d\right]^T \tilde{i}_g = \left[\tilde{i}_q^g \;\; \tilde{i}_d^g\right]^T \tilde{v}_{pcc} = \left[\tilde{v}_q^{pcc} \;\; \tilde{v}_d^{pcc}\right]^T$ and $\tilde{u} = \left[\tilde{m} \;\; \tilde{\psi}\right]^T$. The block matrices used in (A2) can be found in Appendix B. The developed open-loop small-signal model for grid-tied VSIs in (A2) can be used to incorporate any control scheme or grid structure.

Now, the state-space model in (A2) is verified using both simulated and experimentally obtained data. In the case of open-loop studies, the grid circuit can be merged into (A2) via replacing R_2 and L_2 by $R_2 + R_g$ and $L_2 + L_g$ respectively, as well as replacing $\tilde{v}_{pcc}$ by v_g. The circuit simulation is performed in the MATLAB platform making use of circuit components from the SimPowerSystem toolbox. The results in Fig. 15 show that the state-space variables obtained from solving (A2) match the circuit simulation results over a step change in the modulation index, m, from 0.8 to 0.9 at 0.45 second. In solving (A2), M was fixed at 0.8 when $\tilde{m}$ had a 0.1 step change, other circuit parameters are given in Section III.

The dynamic model given in (A2) is also verified against the experimental results, as shown in Fig. 16. The state

variables representing the voltage across the filter capacitor and the line currents being injected to the grid is transformed to the *abc* frame of reference from the *dq* frame model in (A2) and plotted against the experimentally obtained data obtained in the *abc* frame. It can be seen from Fig. 16 that the developed model impressively represents the actual laboratory test results under both steady-state operation and a sudden change in the modulation index from 0.83 to 0.93 at 0.4 second. In addition, the power board of an Allen-Bradly drive, Powerflex 755, was used while the switching signals were generated by an FPGA board and the grid measured signals were fed back through a measurement board and a dSpace 1103 [36].

APPENDIX B

In this appendix, the block matrix elements introduced in the main body of the paper as well as in Appendix A are provided in details. The block matrices of (1) are

$$A_{11} = \begin{bmatrix} -\frac{3R_1+R_f}{3L_1} & -\Omega \\ \Omega & -\frac{3R_1+R_f}{3L_1} \end{bmatrix};$$

$$A_{12} = \begin{bmatrix} -\frac{1}{2L_1} & \frac{\sqrt{3}}{6L_1} \\ -\frac{\sqrt{3}}{6L_1} & -\frac{1}{2L_1} \end{bmatrix};$$

$$A_{13} = \begin{bmatrix} \frac{R_f}{3L_1} & 0 \\ 0 & \frac{R_f}{3L_1} \end{bmatrix}; \quad A_{21} = \begin{bmatrix} \frac{1}{2C_f} & \frac{\sqrt{3}}{6C_f} \\ -\frac{\sqrt{3}}{6C_f} & \frac{1}{2C_f} \end{bmatrix};$$

$$A_{22} = \begin{bmatrix} 0 & -\Omega \\ \Omega & 0 \end{bmatrix}; \quad A_{23} = \begin{bmatrix} -\frac{1}{2C_f} & -\frac{\sqrt{3}}{6C_f} \\ \frac{\sqrt{3}}{6C_f} & -\frac{1}{2C_f} \end{bmatrix};$$

$$A_{31} = \begin{bmatrix} \frac{R_f}{3L_2} & 0 \\ 0 & \frac{R_f}{3L_2} \end{bmatrix}; \quad A_{32} = \begin{bmatrix} \frac{1}{2L_2} & -\frac{\sqrt{3}}{6L_2} \\ \frac{\sqrt{3}}{6L_2} & \frac{1}{2L_2} \end{bmatrix};$$

$$A_{33} = \begin{bmatrix} -\frac{3R_2+R_f}{3L_2} & -\Omega \\ \Omega & -\frac{3R_2+R_f}{3L_2} \end{bmatrix};$$

$$B_{12} = \begin{bmatrix} \frac{V_{dc}\cos(\Psi)}{\sqrt{3}L_1} & \frac{-MV_{dc}\sin(\Psi)}{\sqrt{3}L_1} \\ \frac{-V_{dc}\sin(\Psi)}{\sqrt{3}L_1} & \frac{-MV_{dc}\cos(\Psi)}{\sqrt{3}L_1} \end{bmatrix};$$

$$B_{31} = \begin{bmatrix} -\frac{1}{2L_2} & \frac{\sqrt{3}}{6L_2} \\ -\frac{\sqrt{3}}{6L_2} & -\frac{1}{2L_2} \end{bmatrix}$$

The block matrices modified due to change in state variables from $\tilde{i}_g = \begin{bmatrix} \tilde{i}_q^g & \tilde{i}_d^g \end{bmatrix}^T$ to $\tilde{i}_{gL} = \begin{bmatrix} \tilde{i}_q^{gL} & \tilde{i}_d^{gL} \end{bmatrix}^T$ are given as $A_{13}^L = A_{13}T_L$, $A_{23}^L = A_{23}T_L$, $A_{31}^L = T_L^{-1}A_{31}$, $A_{32}^L = T_L^{-1}A_{32}$, $B_{31}^L = T_L^{-1}B_{31}$, $b_3^L = T_L^{-1}b_3$, and $A_{33}^L = T_L^{-1}A_{33}T_L$, where

$$T_L = \begin{bmatrix} \frac{1}{2} & \frac{-\sqrt{3}}{6} \\ \frac{\sqrt{3}}{6} & \frac{1}{2} \end{bmatrix}$$

The block matrix M, which was introduced in Section II after equation (20), is given below

$$M = \begin{bmatrix} V_{dc}\cos(\Psi) & -MV_{dc}\sin(\Psi) \\ -V_{dc}\sin(\Psi) & -MV_{dc}\cos(\Psi) \end{bmatrix};$$

The following block matrices were first introduced in (18).

$$B_{61} = \frac{1}{T_d}\begin{bmatrix} 1-\frac{K_{p1}K_{p2}I_{qL}}{2} & \frac{-K_{p1}K_{p2}I_{dL}}{2} \\ \frac{-K_{p3}K_{p4}I_{dL}}{2} & 1+\frac{K_{p3}K_{p4}I_{qL}}{2} \end{bmatrix};$$

$$A_{64} = \frac{1}{T_d}\begin{bmatrix} K_{p2} & 0 \\ 0 & K_{p4} \end{bmatrix}; \quad B_{63} = \frac{1}{T_d}\begin{bmatrix} K_{p1}K_{p2} & 0 \\ 0 & K_{p3}K_{p4} \end{bmatrix};$$

$$A_{63} = \frac{1}{T_d}\begin{bmatrix} -K_{p2}-\frac{K_{p1}K_{p2}V_q^{pcc}}{2} & \omega L \\ -\omega L & -K_{p4}-\frac{K_{p3}K_{p4}V_q^{pcc}}{2} \end{bmatrix};$$

$$A_{65} = -A_{66} = \frac{1}{T_d}\begin{bmatrix} 1 & 0 \\ 0 & 1 \end{bmatrix}; \quad B_{43} = \begin{bmatrix} K_{i1} & 0 \\ 0 & K_{i3} \end{bmatrix};$$

$$G_1 = \begin{bmatrix} R_g & \omega L_g \\ -\omega L_g & R_g \end{bmatrix}; \quad G_2 = L_g;$$

The block matrices of (8) are given below

$$B_{41} = \begin{bmatrix} -\frac{K_{i1}I_{qL}}{2} & -\frac{K_{i1}I_{dL}}{2} \\ -\frac{K_{i3}I_{dL}}{2} & \frac{K_{i3}I_{qL}}{2} \end{bmatrix};$$

$$B_{53} = \begin{bmatrix} K_{p1}K_{i2} & 0 \\ 0 & K_{p3}K_{i4} \end{bmatrix};$$

$$A_{43} = \begin{bmatrix} -\frac{K_{i1}V_q^{pcc}}{2} & 0 \\ 0 & -\frac{K_{i3}V_q^{pcc}}{2} \end{bmatrix};$$

$$B_{51} = \begin{bmatrix} \frac{-K_{p1}K_{i2}I_{qL}}{2} & \frac{-K_{p1}K_{i2}I_{dL}}{2} \\ \frac{-K_{p3}K_{i4}I_{dL}}{2} & \frac{K_{p3}K_{i4}I_{qL}}{2} \end{bmatrix};$$

$$A_{54} = \begin{bmatrix} K_{i2} & 0 \\ 0 & K_{i4} \end{bmatrix};$$

$$A_{53} = \begin{bmatrix} -K_{i2}-\frac{K_{p1}K_{i2}V_q^{pcc}}{2} & 0 \\ 0 & -K_{i4}-\frac{K_{p3}K_{i4}V_q^{pcc}}{2} \end{bmatrix}.$$

Also, the block matrices first encountered in (21) are

$$A_{16}^C = B_{12}M^{-1}$$
$$A_{31}^C = A_{31}^L + B_{31}^L(I - G_2B_{31}^L)^{-1}G_2A_{31}^L$$
$$A_{n1}^C = B_{n1}(I - G_2B_{31}^L)^{-1}G_2A_{31}^L, \quad n = 4, 5, 6$$

$$A_{32}^{C} = A_{32}^{L} + B_{31}^{L}(I - G_2 B_{31}^{L})^{-1} G_2 A_{32}^{L}$$
$$A_{n1}^{C} = B_{n1}(I - G_2 B_{31}^{L})^{-1} G_2 A_{32}^{L}, \quad n = 4, 5, 6$$
$$A_{n3}^{C} = A_{n3} + B_{n1}(I - G_2 B_{31}^{L})^{-1}\left(G_1 + G_2 A_{33}^{L}\right), \quad n = 3, 4, 5, 6$$
$$C_{13} = \begin{bmatrix} \frac{V_q^{pcc}}{2} & 0 \\ 0 & \frac{V_q^{pcc}}{2} \end{bmatrix}; \quad D_{11} = \begin{bmatrix} \frac{I_{qL}}{2} & \frac{I_{dL}}{2} \\ \frac{I_{dL}}{2} & -\frac{I_{qL}}{2} \end{bmatrix};$$

Finally, the output, $Z = \begin{bmatrix} P & Q \end{bmatrix}^T$, equation of the full-order system is given by

$$Z = \begin{bmatrix} C_1 & C_2 & C_3 & 0 & 0 & 0 \end{bmatrix} \begin{bmatrix} i_{inv} \\ v_c \\ i_{gL} \\ y_1 \\ y_2 \\ v_{inv} \end{bmatrix} + \begin{bmatrix} D_1 & D_2 & 0 \end{bmatrix} \begin{bmatrix} v_g \\ \omega \\ R^* \end{bmatrix};$$

$$C_n = D_{11}(I - G_2 B_{31}^{L})^{-1} G_2 A_{3n}^{L}, \quad n = 1, 2$$
$$C_3 = C_{13} + D_{11}(I - G_2 B_{31}^{L})^{-1}\left(G_1 + G_2 A_{33}^{L}\right)$$
$$D_1 = D_{11}(I - G_2 B_{31}^{L})^{-1}$$
$$D_2 = D_{11}(I - G_2 B_{31}^{L})^{-1} G_2 b_3^{C}$$

The equations matrices provided in details in this appendix, enable one to duplicate the work presented in this paper.

REFERENCES

[1] J. M. Carrasco *et al.*, "Power-electronic systems for the grid integration of renewable energy sources: A survey," *IEEE Trans. Ind. Electron.*, vol. 53, no. 4, pp. 1002–1016, Jun. 2006.
[2] F. Blaabjerg, Z. Chen, and S. B. Kjaer, "Power electronics as efficient interface in dispersed power generation systems," *IEEE Trans. Power Electron.*, vol. 19, no. 5, pp. 1184–1194, Sep. 2004.
[3] J. Rocabert, A. Luna, F. Blaabjerg, and P. Rodriguez, "Control of power converters in AC microgrids," *IEEE Trans. Power Electron.*, vol. 27, no. 11, pp. 4734–4749, Nov. 2012.
[4] G. Shen, D. Xu, L. Cao, and X. Zhu, "An improved control strategy for grid-connected voltage source inverters with an LCL filter," *IEEE Trans. Power Electron.*, vol. 23, no. 4, pp. 1899–1906, Jul. 2008.
[5] Y. Tang, P. C. Loh, P. Wang, F. H. Choo, and F. Gao, "Exploring inherent damping characteristic of LCL-filters for three-phase grid-connected voltage source inverters," *IEEE Trans. Power Electron.*, vol. 27, no. 3, pp. 1433–1443, Mar. 2012.
[6] J. Yin, S. Duan, and B. Liu, "Stability analysis of grid-connected inverter with LCL filter adopting a digital single-loop controller with inherent damping characteristic," *IEEE Trans. Ind. Informat.*, vol. 9, no. 2, pp. 1104–1112, May 2013.
[7] J. Kukkola, M. Hinkkanen, and K. Zenger, "Observer-based state-space current controller for a grid converter equipped with an LCL filter: Analytical method for direct discrete-time design," *IEEE Trans. Ind. Electron.*, vol. 51, no. 5, pp. 4079–4090, Sep./Oct. 2015.
[8] D. Yang, X. Ruan, and H. Wu, "Impedance shaping of the grid-connected inverter with LCL filter to improve its adaptability to the weak grid condition," *IEEE Trans. Power Electron.*, vol. 29, no. 11, pp. 5795–5805, Nov. 2014.
[9] G. Qi, A. Chen, and J. Chen, "Improved control strategy of interlinking converters with synchronous generator characteristic in islanded hybrid AC/DC microgrid," *CPSS Trans. Power Electron. Appl.*, vol. 2, no. 2, pp. 149–158, Jun. 2017.
[10] C. Zheng, L. Zhou, X. Yu, B. Li, and J. Liu, "Online phase margin compensation strategy for a grid-tied inverter to improve its robustness to grid impedance variation," *IET Power Electron.*, vol. 9, no. 4, pp. 611–620, Mar. 2016.
[11] Y. Huang, X. Yuan, J. Hu, and P. Zhou, "Modeling of VSC connected to weak grid for stability analysis of DC-link voltage control," *IEEE J. Emerg. Sel. Topics Power Electron.*, vol. 3, no. 4, pp. 1193–1204, Dec. 2015.
[12] M. Ashabani and Y. A.-R. I. Mohamed, "Integrating VSCs to weak grids by nonlinear power damping controller with self-synchronization capability," *IEEE Trans. Power Syst.*, vol. 29, no. 2, pp. 805–814, Mar. 2014.
[13] M. Davari and Y. A.-R. I. Mohamed, "Robust vector control of a very weak-grid-connected voltage-source converter considering the phase-locked loop dynamics," *IEEE Trans. Power Electron.*, vol. 32, no. 2, pp. 977–994, Feb. 2017.
[14] M. Zhao, X. Yuan, J. Hu, and Y. Yan, "Voltage dynamics of current control time-scale in a VSC-connected weak grid," *IEEE Trans. Power Syst.*, vol. 31, no. 4, pp. 2925–2937, Jul. 2016.
[15] A. G. Yepes, A. Vidal, O. López, and J. Doval-Gandoy, "Evaluation of techniques for cross-coupling decoupling between orthogonal axes in double synchronous reference frame current control," *IEEE Trans. Ind. Electron.*, vol. 61, no. 7, pp. 3527–3531, Jul. 2014.
[16] S. Wei, Y. Zhou, and Y. Huang, "Synchronous motor-generator pair to enhance small signal and transient stability of power system with high penetration of renewable energy," *IEEE Access*, vol. 5, pp. 11505–11512, 2017.
[17] M. Huang, Y. Peng, C. K. Tse, Y. Liu, J. Sun, and X. Zha, "Bifurcation and large-signal stability analysis of three-phase voltage source converter under grid voltage dips," *IEEE Trans. Power Electron.*, vol. 32, no. 11, pp. 8868–8879, Nov. 2017.
[18] M. Cespedes and J. Sun, "Impedance modeling and analysis of grid-connected voltage-source converters," *IEEE Trans. Power Electron.*, vol. 29, no. 3, pp. 1254–1261, Mar. 2014.
[19] B. Wen, D. Boroyevich, R. Burgos, P. Mattavelli, and Z. Shen, "Analysis of D-Q small-signal impedance of grid-tied inverters," *IEEE Trans. Power Electron.*, vol. 31, no. 1, pp. 675–687, Jan. 2016.
[20] Z. Zhu, G. Geng, and Q. Jiang, "Power system dynamic model reduction based on extended Krylov subspace method," *IEEE Trans. Power Syst.*, vol. 31, no. 6, pp. 4483–4494, Nov. 2016.
[21] C. Wang, H. Yu, P. Li, J. Wu, and C. Ding, "Model order reduction for transient simulation of active distribution networks," *IET Generat., Transmiss. Distrib.*, vol. 9, no. 5, pp. 457–467, Apr. 2015.
[22] A. Ramirez *et al.*, "Application of balanced realizations for model-order reduction of dynamic power system equivalents," *IEEE Trans. Power Del.*, vol. 31, no. 5, pp. 2304–2312, Oct. 2016.
[23] F. A. Alskran, "Dynamic modeling and analysis of the three-phase voltage source inverter under stand-alone and grid-tied modes," M.S. thesis, Dept. Elect. Comput. Eng. College Eng., Kansas State Univ., Manhattan, Kansas, Aug. 2014.
[24] F. Blaabjerg, R. Teodorescu, M. Liserre, and A. V. Timbus, "Overview of control and grid synchronization for distributed power generation systems," *IEEE Trans. Ind. Electron.*, vol. 53, no. 5, pp. 1398–1409, Oct. 2006.
[25] D. S. Ochs, B. Mirafzal, and P. Sotoodeh, "A method of seamless transitions between grid-tied and stand-alone modes of operation for utility-interactive three-phase inverters," *IEEE Trans. Ind. Appl.*, vol. 26, no. 3, pp. 1934–1941, May 2014.
[26] A. Timbus, M. Liserre, R. Teodorescu, P. Rodriguez, and F. Blaabjerg, "Evaluation of current controllers for distributed power generation systems," *IEEE Trans. Power Electron.*, vol. 24, no. 3, pp. 654–664, Mar. 2009.
[27] Y. Wang, X. Wang, F. Blaabjerg, and Z. Chen, "Harmonic instability assessment using state-space modeling and participation analysis in inverter-fed power systems," *IEEE Trans. Ind. Electron.*, vol. 64, no. 1, pp. 806–816, Jan. 2017.
[28] J. Wang, J. Yan, L. Jiang, and J. Zou, "Delay-dependent stability of single-loop controlled grid-connected inverters with LCL filters," *IEEE Trans. Power Electron.*, vol. 31, no. 1, pp. 743–757, Jan. 2016.
[29] V. Mariani, F. Vasca, J. C. Vasquez, and J. M. Guerrero, "Model order reductions for stability analysis of islanded microgrids with droop control," *IEEE Trans. Ind. Electron.*, vol. 62, no. 7, pp. 4344–4354, Jul. 2015.
[30] A. C. Antoulas, D. C. Sorensen, and S. Gugercin, "A survey of model reduction methods for large-scale systems," *Contemp. Math.*, vol. 280, pp. 193–219, Dec. 2000.
[31] D. G. Holmes and T. A. Lipo, *Pulse Width Modulation for Power Converters: Principles and Practice*, 1st ed. New York, NY, USA: Wiley, 2003.
[32] J. A. Sanders and F. Verhulst, *Averaging Methods in Nonlinear Dynamical Systems*. New York, NY, USA: Springer-Verlag, 1985.

[33] A. Singh, A. K. Kaviani, and B. Mirafzal, "On dynamic models and stability analysis of three-phase phasor PWM-based CSI for stand-alone applications," *IEEE Trans. Ind. Electron.*, vol. 62, no. 5, pp. 2698–2707, May 2015.
[34] R. H. Park, "Two-reaction theory of synchronous machines generalized method of analysis—Part I," *Trans. Amer. Inst. Elect. Eng.*, vol. 48, no. 3, pp. 716–727, Jul. 1929.
[35] P. C. Krause, O. Wasynczuk, and S. D. Sudhoff, *Analysis of Electric Machinery and Drive Systems*, 2nd ed. Piscataway, NJ, USA: Wiley, 2002.
[36] J. Lamb, A. Singh, and B. Mirafzal, "Rapid implementation of solid-state based converters in power engineering laboratories," *IEEE Trans. Power Syst.*, vol. 31, no. 4, pp. 2957–2964, Jul. 2016.

ASWAD ADIB (S'14) was born in Chandpur, Bangladesh, in 1988. He received the B.Sc. degree in electrical and electronic engineering from the Bangladesh University of Engineering and Technology, Dhaka, Bangladesh, in 2012. He is currently pursuing the Ph.D. degree with Kansas State University, Manhattan, KS, USA. He was a Software Engineer with the Samsung R&D Institute Bangladesh from 2012 to 2014. His research interests include power electronics, dynamic modeling, and stability analysis of grid-interactive power converters and stability of low-inertia microgrids.

BEHROOZ MIRAFZAL (S'01–M'05–SM'07) received the Ph.D. degree in electrical engineering from Marquette University, Milwaukee, WI, in 2005. From 2005 to 2008, he was with Rockwell Automation/Allen-Bradley, Mequon, WI, as a Senior Development/Project Engineer, where he was involved in research and development related to motor-drive systems. From 2008 to 2011, he was an Assistant Professor with Florida International University, Miami, FL. He is currently an Associate Professor with Kansas State University, Manhattan, KS. He has published over 70 articles in professional journals and conferences and holds four U.S. patents. His current research interests include applications of power electronics in modern energy conversion systems and microgrids.

Dr. Mirafzal was a recipient of the 2008 Second Best IEEE Industry Applications Society Transactions Prize Paper Award published in 2007, the Best 2012 IEEE Power and Energy Society Transactions Prize Paper Award published in 2011, and the 2014 U.S. National Science Foundation CAREER Award. He has served as the Technical Co-Chair of the IEEE IEMDC Conference in 2009. He is currently an Associate Editor of the IEEE TRANSACTIONS ON INDUSTRY APPLICATIONS.

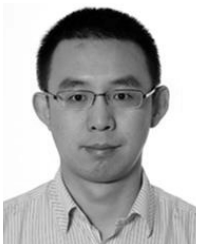

XIONGFEI WANG (S'10–M'13–SM'17) received the B.S. degree in electrical engineering from Yanshan University, Qinhuangdao, China, in 2006, the M.S. degree in electrical engineering from the Harbin Institute of Technology, Harbin, China, in 2008, and the Ph.D. degree in energy technology from Aalborg University, Aalborg, Denmark, in 2013. Since 2009, he has been with Aalborg University, where he is currently an Associate Professor with the Department of Energy Technology. His research interests include modeling and control of grid-connected converters, harmonics stability analysis and control, passive and active filters, and the stability of power electronics for power systems.

Dr. Wang received the Second Prize Paper Award and the Outstanding Reviewer Award of the IEEE TRANSACTIONS ON POWER ELECTRONICS in 2014 and 2017, respectively, the Second Prize Paper Award of the IEEE TRANSACTIONS ON INDUSTRY APPLICATIONS in 2017, and the best paper awards at the IEEE PEDG 2016 and the IEEE PES GM 2017. He serves as an Associate Editor of the IEEE TRANSACTIONS ON POWER ELECTRONICS, the IEEE TRANSACTIONS ON INDUSTRY APPLICATIONS, and the IEEE JOURNAL OF EMERGING AND SELECTED TOPICS IN POWER ELECTRONICS. He is also the Guest Editor for the Special Issue Grid-Connected Power Electronics Systems: Stability, Power Quality, and Protection in the IEEE TRANSACTIONS ON INDUSTRY APPLICATIONS.

FREDE BLAABJERG (S'86–M'88–SM'97–F'03) received the Ph.D. degree in electrical engineering from Aalborg University in 1995. He was with ABB-Scandia, Randers, Denmark, from 1987 to 1988. He became an Assistant Professor in 1992, an Associate Professor in 1996, and a Full Professor of power electronics and drives in 1998 with Aalborg University, where he became a Villum Investigator in 2017.

He has published over 500 journal papers in the fields of power electronics and its applications. He is a co-author of two monographs and an editor of six books in power electronics and its applications. His current research interests include power electronics and its applications, such as in wind turbines, PV systems, reliability, harmonics, and adjustable speed drives.

Dr. Blaabjerg has received 24 IEEE prize paper awards, the IEEE PELS Distinguished Service Award in 2009, the EPE-PEMC Council Award in 2010, the IEEE William E. Newell Power Electronics Award 2014, and the Villum Kann Rasmussen Research Award 2014. He was the Editor-in-Chief of the IEEE TRANSACTIONS ON POWER ELECTRONICS from 2006 to 2012. He has been a Distinguished Lecturer for the IEEE Power Electronics Society from 2005 to 2007 and the IEEE Industry Applications Society from 2010 to 2011 and from 2017 to 2018.

He is nominated by Thomson Reuters to be among the most 250 cited researchers in engineering in the world from 2014 to 2017. In 2017, he became Honoris Causa at University Politehnica Timisoara, Romania.